Graphical Abstract

Comprehensive sensitivity and mechanistic analysis of fuel cell performance under varying operating conditions using RF-Sobol-DRT approach

Bowen Liang, Huanxia Wei, Mengzhu Shen, Yuan Gao, Tong Zhang, Jida Men

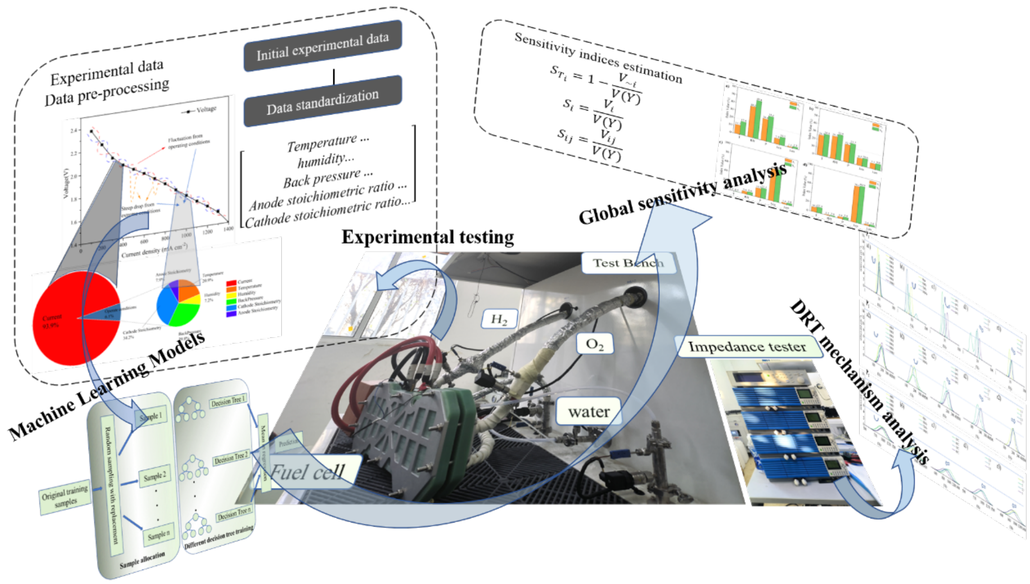

Highlights

Comprehensive sensitivity and mechanistic analysis of fuel cell performance under varying operating conditions using RF-Sobol-DRT approach

Bowen Liang, Huanxia Wei, Mengzhu Shen, Yuan Gao, Tong Zhang, Jida Men

- Machine learning combined with global sensitivity analysis quantifies the impact of operating conditions on fuel cell output.
- DRT technology further identifies the underlying mechanisms behind fuel cell sensitivity to operating conditions by comparing key characteristic peaks.
- The study provides a comprehensive sensitivity analysis, moving from qualitative to quantitative insights, and further to mechanistic understanding.

Comprehensive sensitivity and mechanistic analysis of fuel cell performance under varying operating conditions using RF-Sobol-DRT approach

Bowen Liang[a,b], Huanxia Wei[c], Mengzhu Shen[d], Yuan Gao[a,b,*], Tong Zhang[a,b,e], Jida Men[a,b]

[a] *The New Energy Vehicle Engineering Center, Tongji University, Shanghai, 201804, Shanghai, China*
[b] *School of Automobile Studies, Tongji University, Shanghai, 201804, Shanghai, China*
[c] *Department of Mechanical Engineering, National University of Singapore, 119077, Singapore*
[d] *Department of Mechanical Engineering, Imperial College London, London, SW7-2AZ, UK*
[e] *Yangtze Delta Region Institute, Tsinghua University, Jiaxing, 314006, Zhejiang, China*

Abstract

This study combines Random Forest, Sobol sensitivity analysis, and Distribution of Relaxation Times (DRT) to investigate how five operating conditions affect fuel cell performance: stack temperature, humidity, backpressure, cathode stoichiometry, and anode stoichiometry. By integrating partial experimental data with machine learning methods, a global sensitivity analysis is conducted. The results indicate that fuel cell performance initially increases and then decreases with rising temperature, backpressure, and humidity, while showing a strong positive correlation with cathode stoichiometry. Anode stoichiometry has a relatively minor effect. Quantitative findings reveal that at low current densities, temperature (10–25%), humidity (30–40%), and backpressure (30%) are the dominant factors influencing output voltage. As current density increases, the impact of cathode stoichiometry rises sharply to over 70%. Utilizing the DRT method, the study provides mechanistic insights, revealing that mass transport imposes the greatest impedance on the fuel cell. At low current densities, the fuel cell is primarily influenced by

*Corresponding author.
Email address: yuan.gao@tongji.edu.cn (Yuan Gao)

water-thermal balance affecting mass transport pathways. At higher current densities, increased reaction rates make the cell more sensitive to gas supply conditions, especially cathode stoichiometry. These findings offer valuable insights for optimizing fuel cell efficiency.

Keywords: Global Sensitivity Analysis, Fuel cell, Operating condition, Random Forest, Distribution of Relaxation Times

---

1. Introduction

With the rise of the green economy, the global energy structure is gradually transitioning from fossil fuels to renewable energy sources such as hydrogen, solar, and wind energy Among these, hydrogen energy stands out as one of the most promising energy forms for the future [1]. Fuel cells, which can convert the hydrogen energy of hydrogen into electrical energy, are characterized by their high efficiency and zero emissions, making them the mainstream application of hydrogen energy [2]. Currently, many countries are investing heavily in hydrogen research and deploying fuel cell technologies. These efforts aim to reduce costs, improve production methods, and promote the widespread use of hydrogen-powered systems [3, 4, 5].

The performance of fuel cells is significantly influenced by operational conditions, which are often complex and varied during actual operation [6, 7]. Askaripour using a two-phase flow model, identified key factors affecting fuel cell performance and two-phase flow characteristics, including inlet humidity, the stoichiometric ratio on the anode side, cell pressure and temperature, as well as the distribution of heat sources and sinks [8]. For medium to high current densities, fuel cell performance decreases with increasing cell pressure. Kahveci et al. found that temperature plays a critical role in the performance of proton exchange membrane fuel cells, with performance deteriorating when a certain temperature threshold is exceeded [9]. Additionally, both humidification and heating significantly influence the operational stability of fuel cells, primarily by affecting the membrane hydration state [10]. Xing et al. reported that an initial increase in the stoichiometric flow ratio enhances the limiting current density, but further increases result in diminishing improvements [11]. It is evident that changes in operational conditions have a non-linear and often complex impact on fuel cell performance [12, 13]. Therefore, establishing a quantitative relationship between operational conditions and fuel cell performance remains a challenging task [14, 15]. Fan et al. quantified the effects of catalyst layer gradients, operating conditions, and their interactions on the performance of PEMFCs using Sobol indices [16]. The results indicated that cathode humidity had the greatest impact on output performance among the operating parameters. Goshtasbi et al. developed a physics-based, two-phase, non-isothermal PEM model and performed sensitivity quantification analysis of model parameters using a derivative-based method [17]. Shao et al. conducted a global sensitivity analysis of the electrochemical model of fuel cells by employing a Bayesian sparse polynomial chaos expansion approach [18]. Zhang et al. achieved multi-objective optimization of PEMFC performance by combining orthogonal experimental results with the entropy weight method [19]. Zhou et al. proposed a two-dimensional real-time fuel cell modeling approach and conducted a sensitivity analysis of input parameters using Sobol indices [20]. It can be observed that most of the current quantitative studies rely on physical models for sensitivity analysis. However, these models often fail to accurately reflect the real operational conditions of fuel cells. There is a lack of research focused on the global sensitivity of fuel cell performance to operational conditions under actual operating scenarios.

Furthermore, exploring the internal mechanisms underlying the correlation between operational conditions and fuel cell performance is also a topic of great interest in the field [21, 22]. The Distribution of Relaxation Times (DRT) technique has attracted considerable attention in recent years due to its ability to effectively interpret the dynamic processes within fuel cells without requiring extensive prior knowledge [23, 24, 25]. This method decomposes impedance data based on frequency, extracting characteristic peaks that are associated with different physical processes within the fuel cell. By analyzing these characteristic peaks, researchers can identify key phenomena such as reaction kinetics and mass transport processes occurring in the fuel cell. Weiß et al. were among the first to apply the DRT technique to high-temperature fuel cells, successfully identifying seven distinct characteristic peaks [26]. Subsequently, Bevilacqua et al. used DRT to investigate the effects of anode operating conditions on high-temperature fuel cells, providing further insights into the reaction and mass transfer characteristics within the cells [27]. Heinzmann et al. extended the application of DRT to low-temperature fuel cells, identifying five characteristic peaks and experimentally validating the physical significance of each peak [28]. Yuan et al. further explored the effects of different operating conditions on the variation of DRT peaks and successfully applied DRT to fault diagnosis in fuel cells

[29, 30]. The primary advantage of the DRT technique is its ability to rapidly identify polarization losses without the need for extensive prior knowledge, making it particularly suitable for the study and diagnosis of proton exchange membrane fuel cells.

It can be observed that most of the current quantitative studies rely on physical models for sensitivity analysis. However, these models often fail to accurately reflect the real operational conditions of fuel cells. There is a lack of research focused on the global sensitivity of fuel cell performance to operational conditions under actual operating scenarios. At the same time, sensitivity quantification studies have not been effectively integrated with mechanistic research.

This paper proposes a comprehensive sensitivity analysis framework based on the RF-Sobol-DRT method, bridging the gap in previous research by integrating qualitative, quantitative, and mechanistic studies. Initially, a qualitative analysis is conducted through controlled variable experiments under different operating conditions, revealing the nonlinear relationship between operational parameters and fuel cell performance. Subsequently, a data-driven approach, random forest model, is employed to simulate fuel cell voltage behavior under varying conditions. By combining this approach with the Sobol index, a novel quantitative analysis is performed to assess the sensitivity of fuel cell performance to different operating conditions in real-world scenarios. Finally, the results from the DRT under different conditions are compared to further explain the findings from both the qualitative and quantitative analyses, exploring the underlying mechanisms. The study results provide valuable insights into the internal mechanisms of fuel cells and enhance the understanding of the sensitivity of performance to operational factors.

2. Experimental study

2.1. Experimental setup

This study uses a fuel cell stack containing three commercial membrane electrode assemblies with an effective area of 300 cm^2. The platinum loading of catalyst is 0.35 mg/cm^2 and the thickness of proton exchange membrane is 12 μm. The stack utilizes metal bipolar plates, with a straight-channel flow field on the cathode side and a serpentine flow field on the anode side, featuring an inlet size of 3/8 inches. The stack has been in operation for approximately six months and has experienced degradation, making it more sensitive to variations in operating conditions.

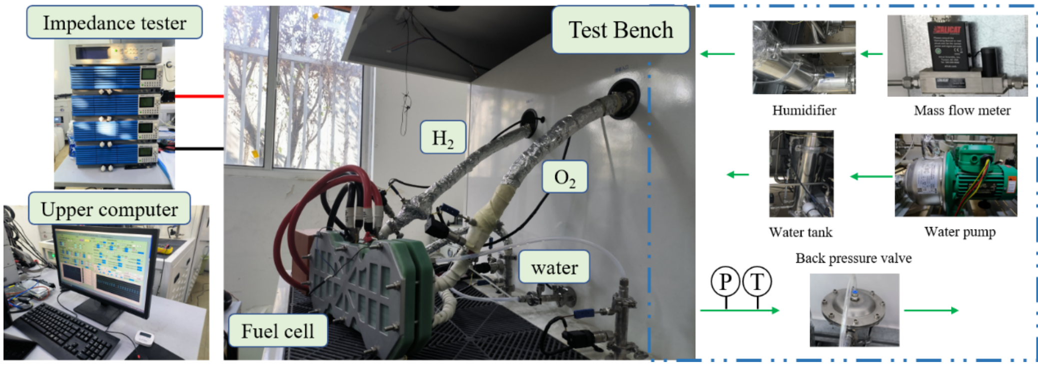

Figure 1: Fuel cell stack and testing equipment

Figure 1 illustrates the test bench setup for a 2 kW fuel cell stack, featuring an electronic load range of 0 to 600 A and a voltage range of 0.1 to 40 V. The stack is water-cooled to regulate its stack temperature. The test bench utilizes two water circuits: an internal deionized water circuit, which humidifies the gas and cools the stack, and an external cooling water circuit, which controls the stack temperature through heat exchange with the internal deionized water. Gas humidification is achieved through a combination of bubbling and spraying techniques, while heating tapes are used to regulate the intake air temperature. The gas humidity is controlled by adjusting the dew point and intake air temperature. The flow rates of hydrogen and air are controlled by high-precision mass flow meters. A diaphragm back-pressure valve at the stack outlet adjusts the gas circuit pressure. Additionally, the anode is equipped with a gas-liquid separator to minimize the impact of anode flooding on fuel cell performance. To further investigate the internal processes of the fuel cell, an AC impedance test is conducted using a KIKUSUI fuel cell impedance meter, which operates over a frequency range of 10 mHz to 20,000 Hz.

2.2. Experimental procedure

To obtain output voltage data under various working conditions, the control variable method is applied in the experimental design process. Standard operating conditions are set at 70 °C, 90% RH, 1 bar pressure, with a stoichiometry of 1.5 for the anode and 3 for the cathode. During each sensitivity test, single operating condition is changed to a preset value, while all other conditions remain at the standard settings. The parameter settings for each test condition are detailed in Table 1. After altering a single test variable, the voltage is recorded once the fuel cell stabilized for 15 minutes. Additionally, in constant current mode, electrochemical impedance spectroscopy (EIS) data are collected with 8% AC perturbation, and the measurement frequency ranges from 0.1 to 20,000 Hz with 10 points per decade. All conditions are measured at different current density levels of 200, 400, 600, and 800 mA/cm^2. To ensure consistent results, the fuel cell is stabilized for 20 minutes prior to each test.

Table 1: Different operating conditions

Parameters	**Standard values**	**Values**
Stack temperature (°C)	70	40, 50, 60, 70, 80
Humidity (%)	90	40, 50, 60, 70, 80, 90, 100
Pressure (kPa)	0	0, 50, 75, 100, 125
Cathode stoichiometry	3	2.0, 2.5, 3.0, 3.5
Anode stoichiometry	1.5	1.5, 2.0, 2.5, 3.0

2.3. DRT method

Impedance Spectroscopy is a powerful tool used to investigate the electrical properties of materials and electrochemical systems. Distribution of Relaxation Times technology is a sophisticated data analysis method applied in impedance spectroscopy. The key idea of DRT is that the response of a fuel cell system can be viewed as the sum of many individual relaxation processes, each characterized by a different time constant. the impedance Z(w) at given frequencies can be calculated in the following expression [31]:

$$Z_{(w)} = R_0 + R_{pol} \int_0^{\infty} \frac{g(\tau)}{1 + jw\tau} d\tau, \tag{1}$$

where R_0 is ohmic impedance, R_{pol} is the polarization resistance, $g(\tau)$ is the distribution function that reveals the contribution of different processes with relaxation time τ. Logarithmic coordinates are often used in practical applications, so the Eq.1 can be written as:

$$Z_{(w)} = R_0 + R_{pol} \int_0^{\infty} \frac{\gamma(ln\tau)}{1 + jw\tau} dln\tau \tag{2}$$

where $\gamma\left(ln\tau\right)=g\left(\tau\right)$.

The method for calculating the DRT in this study primarily utilizes ridge regression and a pseudo-spectral algorithm using radial basis functions [32]. The EIS data must be validated for linearity, time-invariance, and causality using the Kramers-Kronig relations to ensures the reliability and accuracy of the impedance spectra measurements [33]. The difference Δ between the fitted model and the measured data can be used to assess the reproducibility of the measured impedance spectrum:

$$\Delta Re(\omega)=\frac{Z_{Re}\left(\omega\right)-Z^{`}_{Re}}{\left|Z\left(\omega\right)\right|}; \tag{3}$$

$$\Delta Im(\omega)=\frac{Z_{Im}\left(\omega\right)-Z^{`}_{Im}}{\left|Z\left(\omega\right)\right|}, \tag{4}$$

where $Z_{Re}\left(\omega\right)$ and Z_{Im} are the real and imaginary parts of the impedance, respectively. $Z^{`}_{Re}$ and $Z^{`}_{Im}$ are the real and imaginary parts of the fitted impedance, respectively. $\left|Z\left(\omega\right)\right|$ is the real part of the impedance, respectively. ω is the angle frequency.

3. RF-SOBOL method

3.1. Random forest regression

Random Forest Regression is an ensemble learning technique used for both regression and classification tasks [34]. It combines the predictions of multiple decision trees to improve predictive performance and control overfitting. The performance of fuel cells can be well predicted using the Random Forest Regression algorithm, and the influence of each input feature on the output can also be extracted effectively.

For a given dataset $D=\{(x_i,y_i)\}_{i=1}^{N}$ where x_i is the feature vector, and y_i is the target value for the i^{th} data point, the algorithm generates multiple bootstrapped samples from the training data. A bootstrapped sample is created by sampling N data points with replacement from the original dataset. D^b represent the b^{th} bootstrapped dataset.

For each bootstrapped dataset D^b, a decision tree is trained. This involves recursively splitting the dataset into subsets. At each node of the tree, the algorithm randomly selects a subset of features F' from the full set of features F and then chooses the best feature and threshold for splitting based on a

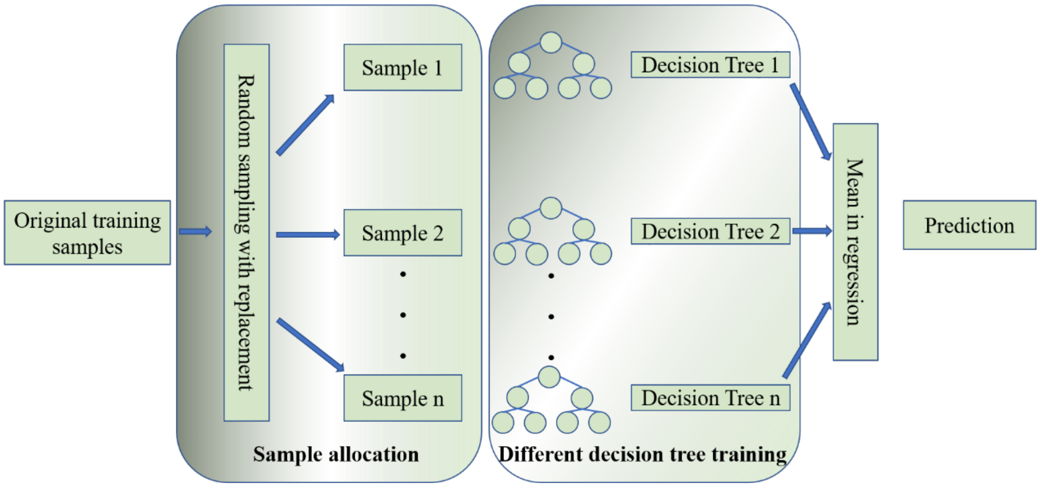

Figure 2: Fuel cell stack and testing equipment

criterion that minimizes the variance in the target values. In regression, the variance reduction criterion is used:

$$V_{ar}\left(D^b\right) = \frac{1}{|D^b|} \sum_{(x_i, y_i) \in D^b} \left(y_i - \bar{y}\right)^2, \tag{5}$$

where $\bar{y}$ is the mean of the target values in subset D^b.

Once all trees are grown, the Random Forest model is ready to make predictions. For a new input x, the prediction is made by averaging the predictions of all individual trees:

$$\hat{y} = \frac{1}{B} \sum_{b=1}^{B} h_b\left(x\right), \tag{6}$$

where B is the total number of trees in the forest, and $h_b\left(x\right)$ is the prediction from the b^{th} tree for input x.

Finally, the algorithm framework is shown in Figure 2.

3.2. SOBOL index

The Sobol Index is a measure used in global sensitivity analysis to quantify the contribution of each input parameter to the variance of the model output [35]. It is used to understand how the uncertainty in each input affects the uncertainty of the output in complex models. Assume a model

$f(\mathbf{X})$ where $\mathbf{X} = (X_1, X_2, \ldots, X_k)$ are k input variables, and the model output $Y = f(\mathbf{X})$ depends on these inputs. The Sobol index is a variance-based method that decomposes the total output variance $\mathrm{Var}(\mathbf{Y})$ into fractions attributed to individual input variables and their interactions:

$$V(\mathbf{Y}) = \sum_{i=1}^{k} V_i + \sum_{1\leq i<j\leq k} V_{ij} + \sum_{1\leq i<j<l\leq k} V_{ijl} + \cdots + V_{12\cdots k}, \tag{7}$$

Where V_i is the variance contribution of the direct effect of the X_i input variables, and V_{ij} is the variance contribution from the interaction between the input variables X_i and X_j. The three main indexes used in this article are as follows.

First-order Sobol index S_i: Direct contribution of X_i to output variance

$$S_i = \frac{V_i}{\mathrm{Var}(\mathbf{Y})}; \tag{8}$$

Second-order Sobol index S_{ij}: Interaction contribution of X_i and X_j

$$S_{ij} = \frac{V_{ij}}{\mathrm{Var}(\mathbf{Y})}; \tag{9}$$

Total Sobol index S_{T_i}: Total contribution of X_i, including all interactions with other variables

$$S_{T_i} = 1 - \frac{V_{\sim i}}{\mathrm{Var}(\mathbf{Y})}, \tag{10}$$

where $V_{\sim i}$ is the variance of the output when X_i is fixed.

3.3. RF-Sobol-DRT method

A fuel cell voltage prediction model based on random forest regression is established using the output voltage of the fuel cell under different operating conditions obtained from experiments. The model inputs include current, pressure, stack temperature, humidity, and stoichiometry of anode and cathode, with the output being the voltage. RF operates by constructing multiple decision trees during training and outputting mean prediction of the individual trees. Its performance largely depends on the proper tuning of several adjustable parameters, which can significantly impact its accuracy, generalization capability, and computational efficiency. The key parameters include the number of estimators, maximum depth, minimum number of samples required to split an internal node, minimum number of samples required to be at a leaf node, and maximum number of features considered for splitting. In this experiment, all input features are required, and thus the maximum number of features is set to include all available features for regression. The default values for the number of estimators, maximum depth, minimum number of samples required to split an internal node, and minimum number of samples required to be at a leaf node are set to 100, 10, 2, and 1, respectively. The mean squared error (MSE) and regression coefficient R^2 obtained from testing when adjusting the number of estimators to 10, 30, 50, 70, 100, 150, 200, and 300 are shown in Table 2.

Table 2: MSE and R^2 for different numbers of estimators

Est	10	30	50	70	100	150	200	300
MSE	0.00848	0.00816	0.00815	0.00860	0.00848	0.00839	0.00852	0.00883
R^2	0.93339	0.93585	0.93591	0.93237	0.93338	0.93407	0.93307	0.93062

It can be observed that the model performs best when the number of trees is set to 50, achieving the lowest prediction error and the highest correlation. Further increasing the number of trees does not improve the model's performance; instead, it reduces computational efficiency. The MSE and R^2 obtained from testing by adjusting the maximum depth to 5, 10, 15, 20, and 25 are shown in Table 3.

Table 3: MSE and R^2 for different maximum depths

Max Depth	5	10	15	20	25
MSE	0.009306	0.008481	0.008431	0.008431	0.008431
R^2	0.926906	0.933389	0.93378	0.93378	0.93378

By adjusting the maximum depth of each tree, it is observed that as the depth increases, the prediction accuracy improves and the error decreases, reaching its peak at a depth of 15. Further increasing the tree depth does not enhance model performance and instead increases the risk of overfitting. Therefore, a depth of 15 is the optimal value for this dataset. The MSE and R^2 obtained from testing by adjusting minimum number of samples required to split an internal node to 2, 4, 6, 8, 10 and minimum number of samples required to be at a leaf node to 1, 2, 3, 4, 5 are shown in Table 4.

Table 4: MSE and R^2 for different minimum samples required to split and minimum samples required at leaf nodes.

Split samples	2	4	6	8	10
MSE	0.008481	0.008602	0.008858	0.00911	0.009644
R^2	0.933389	0.93244	0.930428	0.928449	0.924256
Min. samples	1	2	3	4	5
MSE	0.008481	0.013395	0.013354	0.01326	0.013217
R^2	0.933389	0.894796	0.895111	0.895849	0.896193

These two relatively large values will force the tree to generalize more, preventing model overfitting, but will significantly reduce the model's prediction accuracy. It can be observed that the minimum values of 2 and 1 are more appropriate for the given requirements. Through comparison, the optimal regression model parameters were determined to be 50, 15, 2, and 1, at which point the MSE = 0.811 and R^2 = 0.936.

The RF regression model effectively captures the steady-state behavior of fuel cells during actual operation, providing a solid foundation for global sensitivity analysis. In this study, the RF-Sobol index method was employed to further quantify the impact of key operational conditions, including fuel cell stack temperature, humidity, back pressure, cathode stoichiometry, and anode stoichiometry, on output voltage. To gain deeper insights into the mechanisms by which each operational condition influences output voltage, the Distribution of Relaxation Times (DRT) method was used to analyze the effects of these conditions on internal impedance and kinetic processes. This comprehensive approach completes the analysis chain from qualitative assessment to quantitative evaluation, culminating in mechanistic understanding. The specific methodological workflow is illustrated in Figure 3.

4. Discussion

The following sections systematically analyze the effects of operating conditions (incl. stack temperature, humidity, back pressure, and stoichiometry of anode and cathode) on the output performance of the fuel cell from qualitative, quantitative, and mechanistic perspectives. This analysis reveals the trends, weighting, and underlying mechanisms by which each operating condition impact the output voltage during actual fuel cell operation, providing comprehensive insights for a global sensitivity analysis of fuel cells.

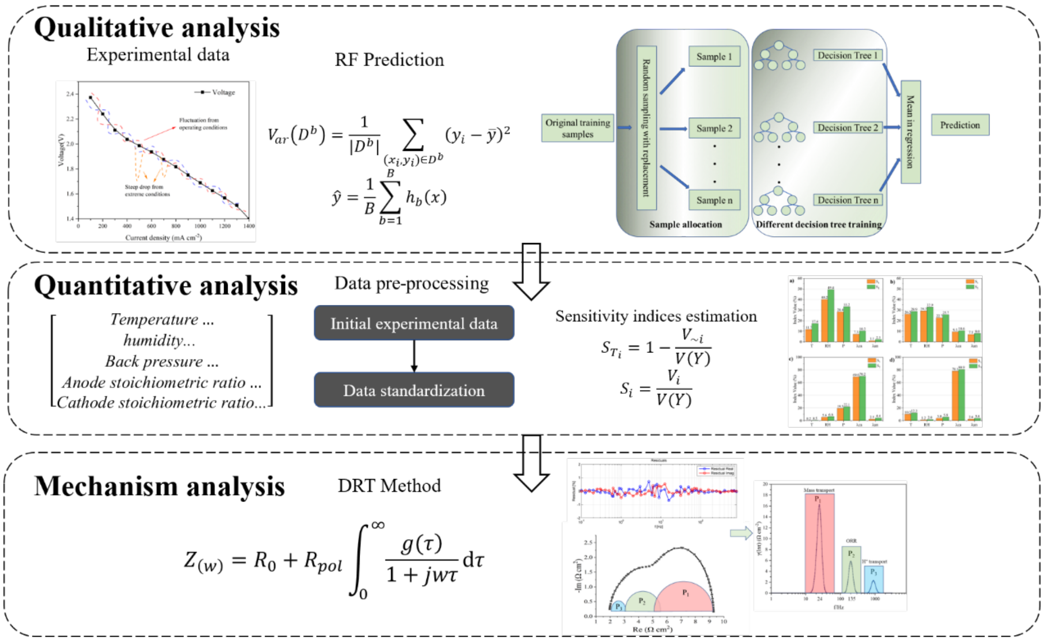

Figure 3: RF-Sobol-DRT method flow chart.

4.1. Qualitative sensitivity analysis

The output voltage under various operation conditions is obtained by experimental testing of control variables, and the RF model is used to perform integrated learning on the data to obtain the predicted values of the output voltage under different operating conditions as shown in Figure 4. The red line is the test result.

From the variations in the red lines in Figure 4 (a1), (b1), (c1), and (d1), it is evident that the output voltage of the fuel cell increases rapidly with rising stack temperature during the experiment. However, the rate of increase gradually slows as the stack temperature continues to rise, reaching a peak at approximately 60 70°C, followed by a slight decline as the stack temperature further increases to 80°C. This trend is observed across different current densities, with the distinction that the stack temperature at which the inflection point occurs decreases as the current density increases. RF prediction model effectively captures the relationship between fuel cell output voltage and stack temperature at various current densities. At 600 mA/cm^2, the effect of stack temperature on the output voltage exhibits minimal fluctuation, except for the lower output voltage observed at 40 °C. The RF model

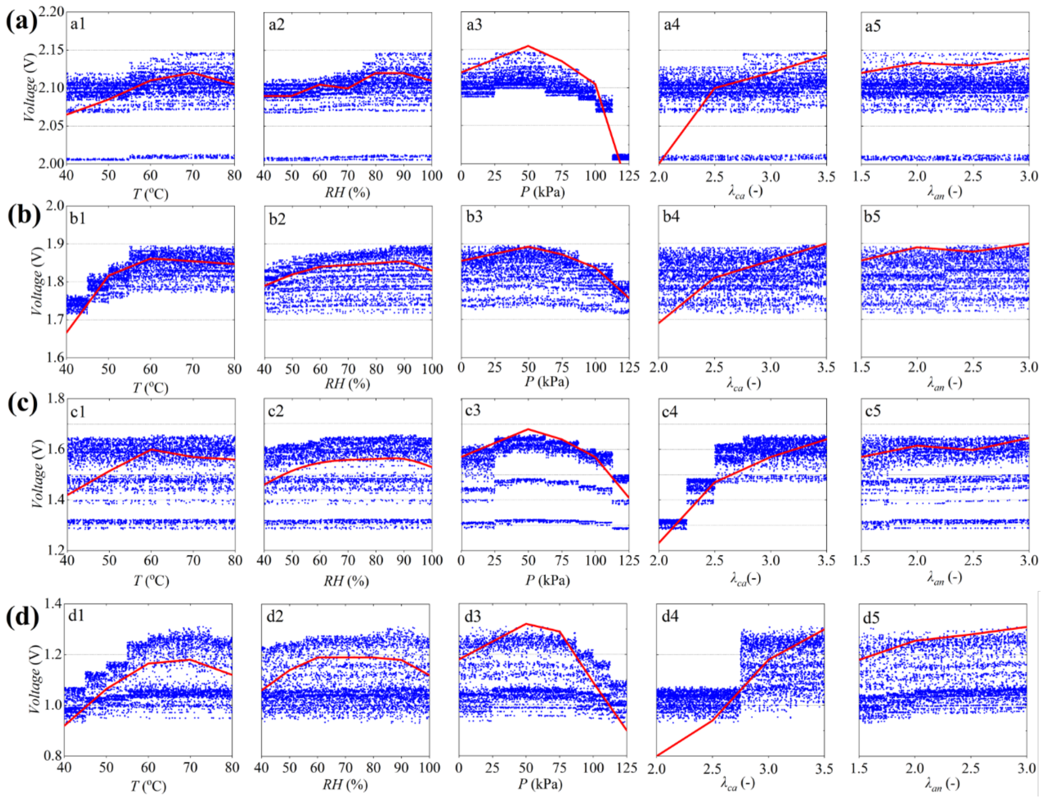

Figure 4: Scatter plot of RF prediction and measured output voltage curves for each operating condition: (a) 200mA/cm^2 ; (b) 400mA/cm^2 ; (c) 600mA/cm^2 ; (d) 800mA/cm^2.

reinforces these characteristics, leading to a weak correlation between stack temperature and output voltage in the scatter plot, which results in a certain degree of deviation. From the Figure 4 (a2), (b2), (c2), and (d2), it can be observed that as humidity increases, the proton exchange membrane becomes more hydrated, resulting in a slight rise in the output voltage. Optimal fuel cell performance is observed at a humidity level of 80–90%, while a slight decrease in output voltage occurs when humidity increases to 100%. This reduction may be attributed to over-humidified gas, which can condense into liquid water, leading to localized flooding and decreased fuel cell performance. The trend in humidity's impact on the fuel cell remains relatively consistent across different current densities. Additionally, the scatter plot generated by the RF model effectively captures these relevant trends. From Figure 4 (a3), (b3), (c3), and (d3), it is observed that as back pressure increases, the partial pressure of the reactant gases rises, accelerating the reaction rate and leading to a continuous increase in the output voltage, which peaks at approximately 50 kPa. However, when the back pressure is further increased, the output voltage begins to decline, and at around 100 kPa, it matches the output voltage observed with no back pressure. If the back pressure is increased beyond this point, the output voltage decreases rapidly. The scatter plot demonstrates that the RF model accurately captures this trend. In Figure 4 (a4), (b4), (c4), and (d4), the output voltage is shown to be positively correlated with the cathode stoichiometry. However, as the stoichiometric ratio increases, the gas supply becomes sufficient, causing the rate of voltage increase to slow. At higher current densities, the demand for gas supply rises, and the cathode stoichiometric ratio continues to have a growing impact on output voltage. The RF model captures this behavior well, though a slight deviation is observed in Figure 4 (b4), similar to the one seen in Figure 4 (c1). In Figure 4 (a5), (b5), (c5), and (d5), it is evident that at low and medium current densities, the anode stoichiometry has minimal effect on the output voltage. As the current density increases, the demand for reactant gases rises, and the overall trend becomes slightly positively correlated. The scatter plot generated by the RF model also exhibits smooth fluctuations.

To further understand the RF model's learning performance for fuel cells under different operating conditions, ICE plots (Figure 5) are generated to illustrate the impact of each feature on the model output. As shown in Figure 5 (a), current is the primary factor influencing fuel cell output, with different current density regions exhibiting distinct characteristics. Figures 5 (b), (c), and (d) show that the RF model effectively captures the nonlinear effects of stack temperature, humidity, and back pressure on output voltage, where the voltage initially increases with the operating conditions but then slows down and even decreases slightly. Additionally, fluctuations become more pronounced with increasing current density. Figures 5 (e) and (f) indicate that the RF model accurately learned the positive correlation between anode and cathode stoichiometry ratios and the output voltage. However, in cases of significant deviations, such as low stack temperatures or low cathode stoichiometry ratios, the model does not perform as well in identifying the feature's impact. Overall, the RF model successfully captured the actual trends and nonlinear relationships between fuel cell output voltage and the various operating conditions.

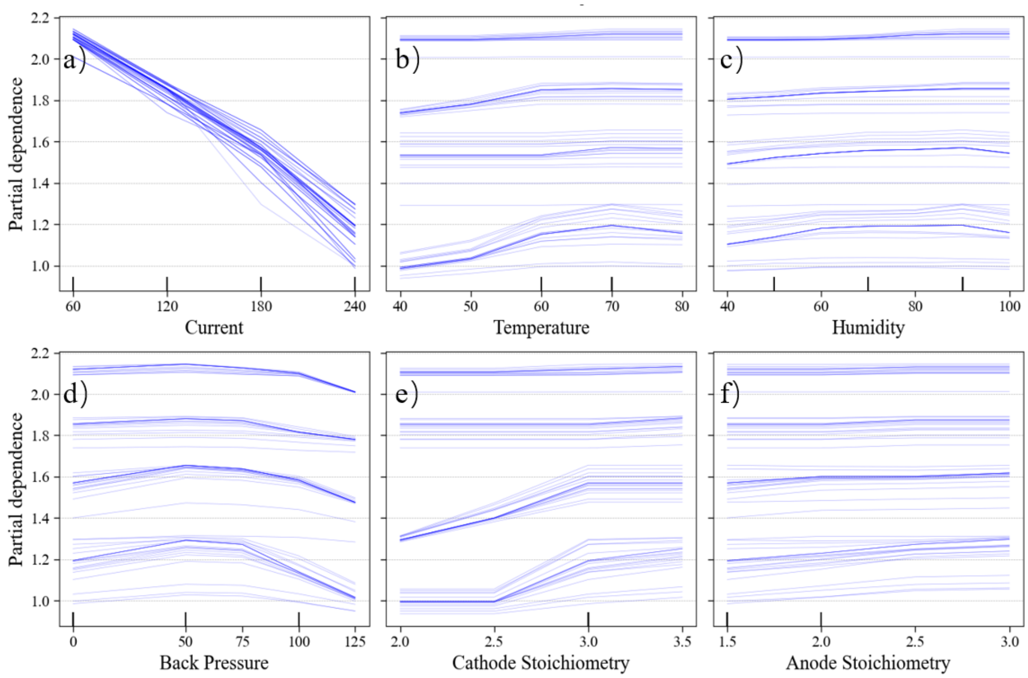

Figure 5: RF model of output voltage under various operating conditions: (a) Current; (b) Stack Temperature; (c) Humidity; (d) Back pressure; (e) Cathode Stoichiometry; (f) Cathode Stoichiometry.

4.2. Globol sensitivity quantitative analysis

In the previous section, a qualitative analysis examines the effects of varying operating conditions on output voltage. Certain operating conditions show a significant influence, with fluctuations exceeding 20% of the output voltage. This section provides the quantitative results of a sensitivity analysis for each operating condition, utilizing a RF model combined with the Sobol index method. Figure 6(a) displays a polarization curve for the fuel cell stack. The output voltage is primarily determined by the current density, which aligns with prior studies. Once a fuel cell system is assembled, the output voltage at a given current density remains stable, with variations in operating conditions causing fluctuations around this value. Under extreme operating conditions, such as flooding or gas starvation, the output voltage experiences a sharp decline due to system malfunction.

The RF model not only enables learning from the input features but also quantifies the contribution of each feature to the prediction model during

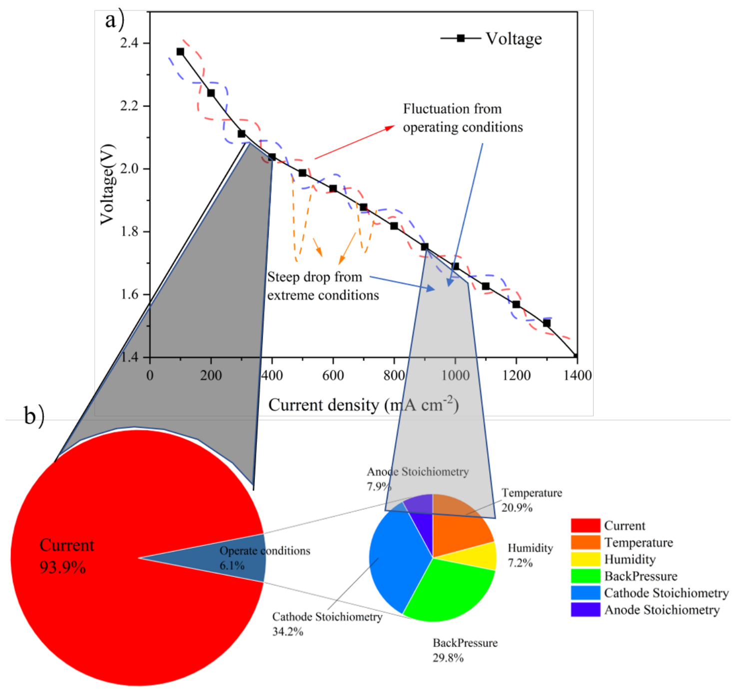

Figure 6: Effect of operating conditions on the polarization curve, (b) Contribution of operating conditions to RF model prediction.

the decision tree construction process. Figure 6(b) presents a pie chart illustrating the contribution of each feature to the prediction model. Current density is the dominant factor, accounting for 93.9% of the predicted output voltage, while operating conditions contribute 6.1%. It is important to note that this 6.1% represents the average contribution across all operating conditions, rather than the specific impact under a given current density. In actual operation, the higher the current density, the more sensitive the fuel cell is to changes in operating conditions. Therefore, for fuel cell systems operating at high current densities, the efficiency improvements resulting from optimizing operating conditions will significantly exceed 6%. A more detailed breakdown of the operating conditions shows that the contributions of stack temperature, humidity, backpressure, cathode stoichiometry, and anode stoichiometry are 20.9%, 7.2%, 29.8%, 34.2%, and 7.9%, respectively. The RF model provides preliminary insights into the overall system behavior, align-

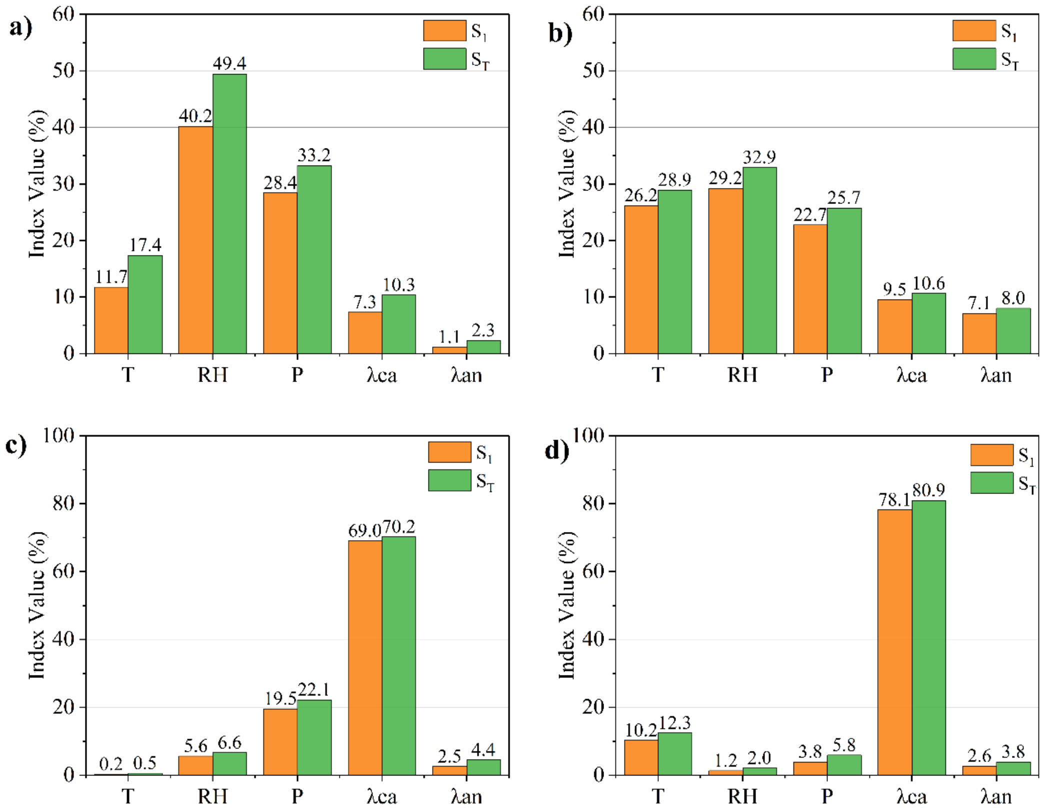

Figure 7: Sobol index results at different current densities: (a) 200mA/cm^2 ; (b) 400mA/cm^2 ; (c) 600mA/cm^2 ; (d) 800mA/cm^2.

ing with the observed performance of fuel cells. However, it does not offer a detailed quantification of the influence of operating conditions on output voltage under fixed current densities. To achieve this, further analysis using the Sobol index method quantifies the effects of each operating condition under different current density scenarios.

Global sensitivity analysis is commonly used for input analysis in models, but it often requires a large amount of data, making it impractical for experimental purposes. To address this, the RF model is being used to simulate the output voltage trends of fuel cells under different operating conditions. Combined with the Sobol index method, this innovative approach enables global sensitivity analysis under experimental conditions. The Sobol index quantifies the influence of inputs by measuring accumulated variance, meaning that extreme operating conditions, which introduce higher variance, can amplify the impact of certain factors and lead to results deviating from real-world observations. Therefore, selecting a reasonable input range is crucial. Since the RF model performs poorly in predicting extreme conditions, the outliers identified in Figure 4 are discarded. The selected ranges for Sobol index calculations are 50–80°C for stack temperature, 40–100% for humidity, 0–100 kPa for back pressure, 2.5–3.5 for cathode stoichiometry ratio, and 1.5–3 for anode stoichiometry ratio. These ranges correspond to optimal fuel cell operation with minimal impact from faults. The calculation results are shown in Figure 7.

According to Figure 7(a), at a low current density of 200 mA/cm^2, the primary factors influencing fuel cell performance are humidity, back pressure, and stack temperature, with first-order Sobol indices (S1) of 40.2%, 28.4%, and 11.7%, respectively. At this low current density, the fuel cell operates with relatively ample gas supply and is more sensitive to internal changes in humidity, back pressure, and stack temperature. The total Sobol indices (ST) for humidity, back pressure, and stack temperature are 49.4%, 33.2%, and 17.4%, respectively. The differences between S1 and ST indicate significant interaction effects between operating conditions. The influence of anode and cathode stoichiometry ratios is much lower, at 7.3% and 1.1%, respectively. As the current density increases to 400 mA/cm^2, shown in Figure 7(b), humidity, back pressure, and stack temperature remain the key influencing factors, contributing 29.2%, 22.7%, and 26.2%, respectively. However, the influence of humidity decreases, while stack temperature's impact increases significantly. The contribution of anode and cathode stoichiometry ratios also increases but remains below 10%. At this intermediate current density, fuel cells still require lower gas supply, and humidity and stack temperature play a significant role. However, as the current density increases, the influence of stack temperature and humidity diminishes, while the effects of back pressure and stoichiometry ratios grow. The gradually decreasing difference between S1 and ST indicates a reduction in the synergistic effect between the operating conditions. At 600 mA/cm^2, Figure 7(c) shows that the cathode stoichiometry ratio and back pressure become the dominant factors, contributing 69% and 19.5%, respectively, while the influence of stack temperature and humidity drops below 8%. Further increasing the current density, as shown in Figure 7(d), makes the cathode stoichiometry ratio the most critical factor, accounting for over 70% of the total influence, with all other operating conditions contributing less than 10%. This shift is due to the higher gas supply demand at elevated current densities, especially

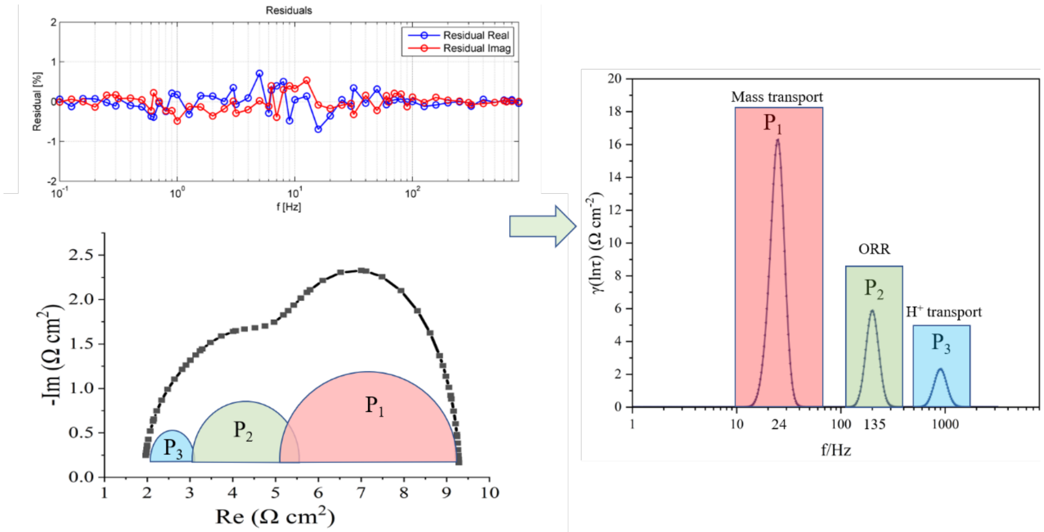

Figure 8: Principle of EIS conversion to DRT and interpretation of DRT Peaks.

for the cathode reaction, which is the rate-limiting step in fuel cell performance. Consequently, changes in the cathode stoichiometry ratio become increasingly important. The diminishing influence of stack temperature and humidity at higher current densities may be associated with internal heat and water production within the fuel cell stack.

In conclusion, when operating at low to moderate current densities, optimizing thermal and water management is crucial for fuel cell performance. As the current density increases, the focus should shift toward managing the air supply, particularly by monitoring changes in the cathode stoichiometry ratio, to ensure sufficient reactant supply and optimal performance.

4.3. Sensitivity analysis of internal mechanisms

The impedance results from the EIS test, as shown in Figure 8, typically require a comprehensive understanding of electrochemical impedance principles and are sensitive to the choice of initial parameters used in equivalent circuit modeling. In contrast, the Distribution of Relaxation Times offers a model-free approach for direct impedance analysis, providing valuable insights into the underlying dynamics Based on the K-K validation, the measurement error of the impedance is less than 1%, which meets the requirements for DRT transformation.

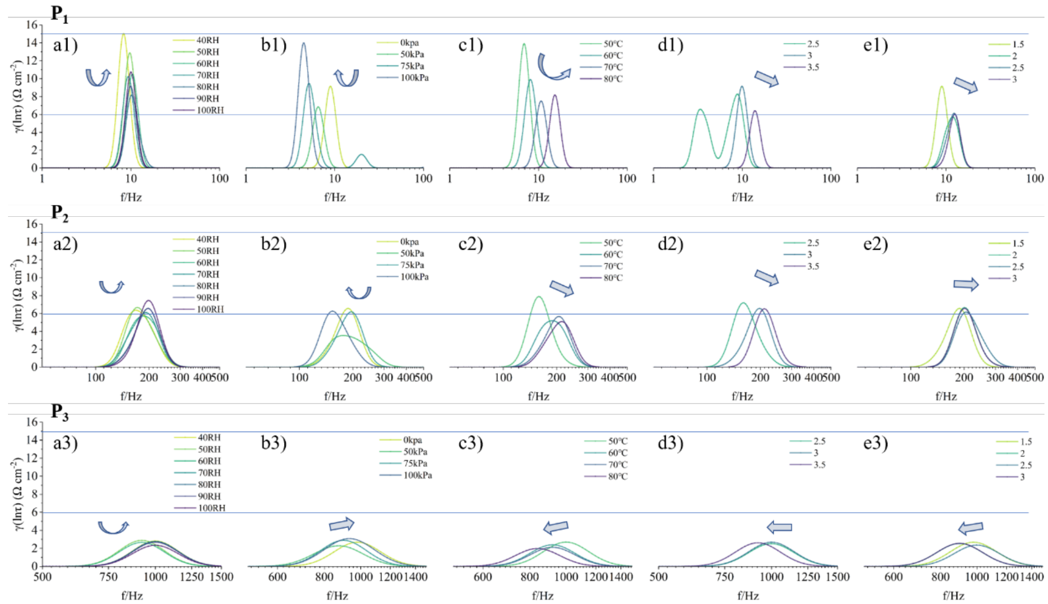

Figure 9: Impact of operation conditions on P_1, P_2, and P_3 peaks in DRT under low current density: (a) Humidity, (b) Backpressure, (c) Stack Temperature, (d) Cathode Stoichiometry, and (e) Anode Stoichiometry.

The DRT analysis results are shown on the right side of Figure 8, revealing three primary peaks. The first peak appears around 10 Hz and is mainly associated with mass transport on the cathode side of the fuel cell. This prominent peak indicates the tested fuel cell is highly sensitive to changes in mass transport. The second peak, observed near 100 Hz, is related to the electrochemical reactions occurring at the cathode. The third and smallest peak, around 1000 Hz, corresponds to proton transport. These conclusions have been confirmed in several studies, supporting further interpretation of the sensitivity of fuel cell operating conditions. As shown in Figure 7, the relevant changes are mainly concentrated at current densities of 200 and 600 mA/cm^2, where the impedance spectra data are most reliable with minimal noise. Therefore, the discussion focuses on the DRT results under these current density conditions. By comparing the effects of various operating conditions on the DRT peaks, the intrinsic mechanism underlying the sensitivity of the fuel cell to different operating conditions at varying current densities is analyzed.

As shown in Figure 9, by examining the impact of various parameters on the three characteristic peaks (P_1, P_2, P_3) of DRT, a deeper understanding is gained regarding each parameter's effect on gas diffusion, cathode reaction kinetics, and proton transport. When comparing the changes in P_1 and P_2 peaks in Figure 9, humidity exhibits the most pronounced impact on fuel cell performance. The results indicate that increasing RH from 40% to 70% significantly reduces the P_1 peak from approximately 15 $\Omega \cdot \mathrm{cm}^2$ to around 8 $\Omega \cdot \mathrm{cm}^2$, showing a more pronounced effect compared to other operating conditions. This is consistent with the conclusion in Figure 7(a). This reduction indicates that as gas humidity increases, the proton exchange membrane and catalyst layer become hydrated, positively impacting the formation of internal transport pathways and enhancing catalyst activity. However, when humidity exceeds 70%, both P_1 and P_2 peaks begin to rise again. This suggests that excessive humidity can lead to water flooding, where liquid water accumulation in the gas diffusion and catalyst layers obstructs reactant gas transport.

Back pressure is another key factor influencing fuel cell performance, with a clear impact on all three characteristic peaks. As back pressure increases from 0 to 50 kPa, both P_1, P_2, and P_3 peaks drop significantly in Figures 9(b1), 9(b2), and 9(b3). This indicates the partial pressure of the reactant gases rises, which improves gas diffusion efficiency and increases reactant concentration. Consequently, the overall performance of the fuel cell is enhanced. However, when the back pressure is further increased beyond 75 kPa, both P_1 and P_2 peaks start to rise again. As observed in Figures 9(b1), 9(b2), and 9(b3), the P_1 peak significantly increases from 7 $\Omega \cdot \mathrm{cm}^2$ to 14 $\Omega \cdot \mathrm{cm}^2$, while the P_2 and P_3 peaks return to their levels seen under no back pressure. This rise indicates that excessive back pressure can lead to issues with gas diffusion, particularly in the GDL and catalyst layers. High back pressure can hinder the removal of water from the GDL, exacerbating water flooding and leading to increased diffusion resistance. Additionally, the increased pressure may cause compression of the porous layers, reducing gas permeability and further impeding gas transport to the catalyst sites.

Comparing Figures 9(b1) and 9(c1), the P_1 peak shows a similar trend with stack temperature variations as it does with back pressure, but the negative effects of increasing stack temperature are relatively weaker, resulting in a more gradual change compared to back pressure. Additionally, from the comparison of the P_2 peak in Figure 9, it is observed that when the stack temperature exceeds 60°C, the P_2 peak remains almost unchanged. This further validates the accuracy of the RF-Sobol method. As stack temperature increases from 40°C to 70°C, both P_1 and P_2 peaks decrease. This shift indicates accelerated reaction kinetics at higher stack temperature, as the increased thermal energy promotes faster charge transfer reactions and enhances the activity of the catalysts. The reduction in impedance in both the low- and mid-frequency ranges reflects improved ORR kinetics and gas diffusion rates at elevated stack temperature. In Figures 9(c1) and 9(c2), when the temperature exceeds 70°C, the P_1 and P_2 peaks begin to rise again, suggesting that there is a threshold for the improvement of fuel cell output voltage with increasing stack temperature. When this threshold is exceeded, stack temperature starts to have adverse effects, likely due to the drying of the gas diffusion layer at higher stack temperature, which leads to insufficient local gas supply and a reduction in the oxygen reaction rate. In Figure 9(c3), the P_3 peak shows a continuous decline as stack temperature increases, indicating enhanced proton transport at higher stack temperatures. This is consistent with the expectation that increased thermal energy reduces the resistance to proton movement through the hydrated membrane, thereby improving proton conductivity.

As shown in Figures 9(d1), 9(d2), and 9(d3), the P_1 peak decreases with an increasing cathode stoichiometric ratio, while the P_2 and P_3 peaks show minimal changes, indicating improved gas diffusion and reaction kinetics due to the increased availability of oxygen at the cathode catalyst sites. However, because the fuel cell operates at low current density and thus has a lower demand for reactant gases, the fluctuations in peak values with respect to the cathode stoichiometric ratio are less pronounced compared to those observed with changes in stack temperature and back pressure. Comparing Figures 9(d1) and 9(e1), as well as 9(d2) and 9(e2), it is evident that changes in the anode stoichiometric ratio have a much smaller impact on the P_1 and P_2 peaks compared to the cathode stoichiometric ratio. This is expected, as the cathode reaction is the rate-determining step in fuel cell performance.

As mentioned earlier, with increasing current density, the fuel cell stack's demand for reactant gases rises. As shown in Figure 7(c), the influence of gas supply-related operating conditions becomes more significant, with the cathode stoichiometric ratio and back pressure emerging as the primary influencing factors. This is further confirmed in Figure 10. Compared to Figure 9, the P_1 peak rises significantly by approximately 5 $\Omega \cdot \mathrm{cm}^2$, indicating a substantial increase in mass transport resistance. At this stage, the cathode stoichiometric ratio becomes the dominant factor. As shown in Figures 9(a1) and 9(a2), increasing the cathode stoichiometric ratio leads to a marked re-

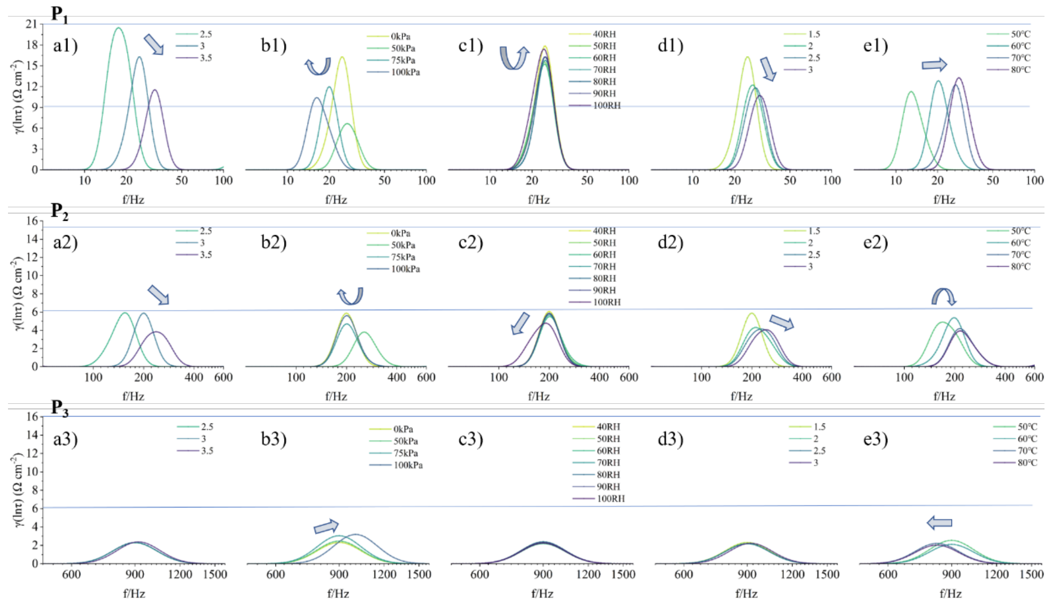

Figure 10: Impact of operation conditions on P_1, P_2, and P_3 peaks in DRT under low current density: (a) Cathode Stoichiometry, (b) Backpressure, (c) Humidity, (d) Anode Stoichiometry and (e) Stack temperature.

duction in the P_1 peak from around 21 $\Omega \cdot cm^2$ to 10 $\Omega \cdot cm^2$, a change far greater than that observed for other operating conditions. Meanwhile, the P_2 peak shows a slight decrease. This explains the approximately 70% contribution of the first-order Sobol index, as increasing the cathode stoichiometric ratio not only facilitates mass transport but also enhances the cathode reaction rate.

As seen in Figures 9(b1) and 9(b2), with the increase in back pressure to 50 kPa, the P_1 peak decreases significantly, from 16 $\Omega \cdot cm^2$ to 7 $\Omega \cdot cm^2$, while the P_2 peak shows a slight decline. This pronounced reduction in the P_1 peak can be attributed to the increased partial pressure of the reactant gases, particularly oxygen at the cathode. Higher back pressure raises the gas concentration, which improves diffusion through the GDL and enhances the availability of oxygen at the catalyst sites. The slight reduction in the P_2 peak is likely due to the enhanced reaction kinetics resulting from improved oxygen concentration at the catalyst, which facilitates faster charge transfer processes. The benefits of increasing back pressure eventually diminish as its adverse effects—such as water flooding and increased gas diffusion resistance—begin to outweigh the advantages. This leads to an increase in all peaks, particularly P_1.

As shown in Figures 10(c1), 10(c2), 10(e1), and 10(e2), the effects of humidity and stack temperature variations on the P_1 and P_2 peaks are relatively gradual compared to the impact of back pressure. The influence of stack temperature and humidity on the P_1 peak is less pronounced at higher current densities than it is at lower current densities. This can be attributed to the increased water and heat generation inside the fuel cell at elevated current densities, which helps maintain a more stable internal water-heat balance. As a result, the fuel cell's sensitivity to external variations in stack temperature and humidity decreases.

In Figures 10(d1) and 10(d2), the impedance is higher at lower anode stoichiometry ratios, but as the anode stoichiometry increases, the P_1 and P_2 peaks decrease and then level off. The effect of the anode stoichiometry ratio on fuel cell performance is relatively straightforward: while increasing the anode stoichiometric ratio reduces gas transport resistance and slightly improves output, the overall effect is not as significant as other operating parameters. Since the hydrogen reaction kinetics are typically not rate-limiting under typical operating conditions, further increases in the anode stoichiometry beyond an optimal point yield little additional performance improvement.

Additionally, as observed in Figure 10, the P_3 peak remains largely unchanged under various operating conditions. This indicates that proton transport has reached a stable and optimal state, with minimal susceptibility to external disturbances such as changes in humidity, stack temperature, or gas supply. The stability of the P_3 peak suggests that proton conductivity within the membrane is well-maintained, likely due to sufficient membrane hydration and proper water management, which ensures consistent proton transport across a wide range of conditions.

5. Conclusion

In conclusion, the study provides a comprehensive evaluation of the impact of key operating conditions—temperature, humidity, backpressure, and stoichiometry—on fuel cell performance using an innovative combination of Random Forest, Sobol sensitivity analysis, and DRT. This work yields the following conclusions:

1. The output voltage of the fuel cell shows an initial increase and subsequent decrease as stack temperature, humidity, and backpressure increase. The

optimal fuel cell performance is observed at a stack temperature of around 70°C, humidity of approximately 90%, and a backpressure of 50 kPa. The output voltage exhibits a strong positive correlation with cathode stoichiometry, while the effect of anode stoichiometry on output voltage is relatively small.

2. The Sobol sensitivity analysis reveals that at low current densities, fuel cell performance is primarily influenced by temperature, humidity, and backpressure, with their contributions being 15–25%, 30–40%, and approximately 30%, respectively. There is also significant interaction between operating conditions. As current density increases, the demand for gas supply rises, making cathode stoichiometry and backpressure the dominant factors. Particularly, the impact of cathode stoichiometry exceeds 70% as current density increases.
3. Mechanistic analysis shows that the fuel cell used in this study is predominantly influenced by mass transport impedance. At low current densities, the fuel cell is significantly affected by water-thermal balance and the establishment of transport pathways, as gas demand is lower. At higher current densities, the increased production of water and heat reduces sensitivity to changes in stack temperature and humidity, while gas supply-related factors, such as cathode stoichiometry and backpressure, become more dominant.

Declarations

- **Funding:**
  This research is supported by the National Natural Science Foundation of China (Grant No: 22279091) and the Fundamental Research Funds for the Central Universities.

- **Conflicts of interest:**
  The authors have no conflicts of interest to declare that are relevant to the content of this article.

- **Data availability:**
  Data will be made available on request.

References

[1] D. B. Pal, A. Singh, A. Bhatnagar, A review on biomass based hydrogen production technologies, International Journal of Hydrogen Energy 47 (2022) 1461–1480. doi:10.1016/j.ijhydene.2021.10.124.

[2] M. Singh, M. K. Singla, S. Beryozkina, J. Gupta, M. Safaraliev, Hydrogen vehicles and hydrogen as a fuel for vehicles: A-state-of-the-art review, International Journal of Hydrogen Energy 64 (2024) 1001–1010. doi:10.1016/j.ijhydene.2024.03.325.

[3] J. Lu, A. Zahedi, C. Yang, M. Wang, B. Peng, Building the hydrogen economy in china: Drivers, resources and technologies, Renewable and Sustainable Energy Reviews 23 (2013) 543–556. doi:10.1016/j.rser.2013.02.042.

[4] K. Shahzad, I. Iqbal Cheema, Low-carbon technologies in automotive industry and decarbonizing transport, Journal of Power Sources 591 (2024) 233888. doi:10.1016/j.jpowsour.2023.233888.

[5] P. Gupta, B. Toksha, M. Rahaman, A critical review on hydrogen based fuel cell technology and applications, CHEMICAL RECORD 24 (2024). doi:10.1002/tcr.202300295.

[6] J.-H. Jang, H.-C. Chiu, W.-M. Yan, W.-L. Sun, Effects of operating conditions on the performances of individual cell and stack of pem fuel cell, Journal of Power Sources 180 (2008) 476–483. doi:10.1016/j.jpowsour.2008.02.001.

[7] A. Kazim, Exergy analysis of a pem fuel cell at variable operating conditions, Energy Conversion and Management 45 (2004) 1949–1961. doi:10.1016/j.enconman.2003.09.030.

[8] H. Askaripour, Effect of operating conditions on the performance of a pem fuel cell, International Journal of Heat and Mass Transfer 144 (2019) 118705. doi:10.1016/j.ijheatmasstransfer.2019.118705.

[9] E. E. Kahveci, I. Taymaz, Assessment of single-serpentine pem fuel cell model developed by computational fluid dynamics, Fuel 217 (2018) 51–58. doi:10.1016/j.fuel.2017.12.073.

[10] A. B. J. N, A. K. Sen, S. K. Das, Effect of humidification and cell heating on the operational stability of polymer electrolyte membrane fuel cell, International Journal of Hydrogen Energy 48 (2023) 35267–35279. doi:10.1016/j.ijhydene.2023.05.269.

[11] L. Xing, et al., Numerical study of the effect of relative humidity and stoichiometric flow ratio on pem (proton exchange membrane) fuel cell performance with various channel lengths: An anode partial flooding modelling, Energy 106 (2016) 631–645. doi:10.1016/j.energy.2016.03.105.

[12] Y. Shao, et al., New insights into steady-state multiplicity in polymer electrolyte membrane fuel cell, Journal of Power Sources 554 (2023) 232328. doi:10.1016/j.jpowsour.2022.232328.

[13] C. Damour, M. Benne, B. Grondin-Perez, J.-P. Chabriat, B. G. Pollet, A novel non-linear model-based control strategy to improve pemfc water management – the flatness-based approach, International Journal of Hydrogen Energy 40 (2015) 2371–2376. doi:10.1016/j.ijhydene.2014.12.052.

[14] B. Laoun, A. M. Kannan, Variance-based global sensitivity analysis of the performance of a proton exchange membrane water electrolyzer, International Journal of Hydrogen Energy 85 (2024) 440–456. doi:10.1016/j.ijhydene.2024.08.233.

[15] B. Laoun, M. W. Naceur, A. Khellaf, A. M. Kannan, Global sensitivity analysis of proton exchange membrane fuel cell model, International Journal of Hydrogen Energy 41 (2016) 9521–9528. doi:10.1016/j.ijhydene.2016.04.046.

[16] R. Fan, G. Chang, Y. Xu, J. Xu, Investigating and quantifying the effects of catalyst layer gradients, operating conditions, and their interactions on pemfc performance through global sensitivity analysis, Energy 290 (2024) 130128. doi:10.1016/j.energy.2023.130128.

[17] A. Goshtasbi, J. Chen, J. R. Waldecker, S. Hirano, T. Ersal, Effective parameterization of pem fuel cell models—part i: Sensitivity analysis and parameter identifiability, Journal of The Electrochemical Society 167 (2020) 044504. doi:10.1149/1945-7111/ab7091.

[18] Q. Shao, et al., Global sensitivity analysis of solid oxide fuel cells with bayesian sparse polynomial chaos expansions, Applied Energy 260 (2020) 114318. doi:10.1016/j.apenergy.2019.114318.

[19] S. Zhang, et al., Multi-objective optimization and evaluation of pemfc performance based on orthogonal experiment and entropy weight method, Energy Conversion and Management 291 (2023) 117310. doi:10.1016/j.enconman.2023.117310.

[20] D. Zhou, et al., Global parameters sensitivity analysis and development of a two-dimensional real-time model of proton-exchange-membrane fuel cells, Energy Conversion and Management 162 (2018) 276–292. doi:10.1016/j.enconman.2018.02.036.

[21] B. Xie, et al., Large-scale three-dimensional simulation of proton exchange membrane fuel cell considering detailed water transition mechanism, Applied Energy 331 (2023) 120469. doi:10.1016/j.apenergy.2022.120469.

[22] K. Jiao, X. Li, Water transport in polymer electrolyte membrane fuel cells, Progress in Energy and Combustion Science 37 (2011) 221–291. doi:10.1016/j.pecs.2010.06.002.

[23] C. Wang, et al., High-precision identification of polarization processes of proton exchange membrane fuel cells through relaxation time analysis: Targeted experimental design and verification, Applied Energy 367 (2024) 123377. doi:10.1016/j.apenergy.2024.123377.

[24] D.-H. Kim, H.-S. Jung, D. H. Kim, C. Pak, Using distribution of relaxation times to separate the impedances in the membrane electrode assembly for high-temperature polymer electrolyte membrane fuel cells, International Journal of Hydrogen Energy 62 (2024) 389–396. doi:10.1016/j.ijhydene.2024.03.041.

[25] S. Nasarre Artigas, H. Xu, F. Mack, Use of distribution of relaxation times analysis as an in-situ diagnostic tool for water management in pem fuel cells applications, Journal of Power Sources 600 (2024) 234179. doi:10.1016/j.jpowsour.2024.234179.

[26] A. Weiß, S. Schindler, S. Galbiati, M. A. Danzer, R. Zeis, Distribution of relaxation times analysis of high-temperature pem fuel

cell impedance spectra, Electrochimica Acta 230 (2017) 391–398. doi:10.1016/j.electacta.2017.02.011.

[27] N. Bevilacqua, M. A. Schmid, R. Zeis, Understanding the role of the anode on the polarization losses in high-temperature polymer electrolyte membrane fuel cells using the distribution of relaxation times analysis, Journal of Power Sources 471 (2020). doi:10.1016/j.jpowsour.2020.228469.

[28] M. Heinzmann, A. Weber, E. Ivers-Tiffée, Advanced impedance study of polymer electrolyte membrane single cells by means of distribution of relaxation times, Journal of Power Sources 402 (2018) 24–33. doi:10.1016/j.jpowsour.2018.09.004.

[29] H. Yuan, et al., Understanding dynamic behavior of proton exchange membrane fuel cell in the view of internal dynamics based on impedance, Chemical Engineering Journal 431 (2022). doi:10.1016/j.cej.2021.134035.

[30] H. Yuan, H. Dai, P. Ming, X. Wang, X. Wei, Quantitative analysis of internal polarization dynamics for polymer electrolyte membrane fuel cell by distribution of relaxation times of impedance, Applied Energy 303 (2021). doi:10.1016/j.apenergy.2021.117640.

[31] F. Ciucci, Modeling electrochemical impedance spectroscopy, Current Opinion in Electrochemistry 13 (2019) 132–139. doi:10.1016/j.coelec.2018.12.003.

[32] T. H. Wan, M. Saccoccio, C. Chen, F. Ciucci, Influence of the discretization methods on the distribution of relaxation times deconvolution: Implementing radial basis functions with drttools, Electrochimica Acta 184 (2015) 483–499. doi:10.1016/j.electacta.2015.09.097.

[33] M. Schönleber, D. Klotz, E. Ivers-Tiffée, A method for improving the robustness of linear kramers-kronig validity tests, Electrochimica Acta 131 (2014) 20–27. doi:10.1016/j.electacta.2014.01.034.

[34] L. Breiman, Random forests, Machine Learning 45 (2001) 5–32. doi:10.1023/A:1010933404324.

[35] A. Saltelli, et al., Variance based sensitivity analysis of model output. design and estimator for the total sensitivity index, Computer Physics Communications 181 (2010) 259–270. doi:10.1016/j.cpc.2009.09.018.